Cell Reports
Physical Science

Article

Manipulating trapped air bubbles in ice for message storage in cold regions

Graphical abstract

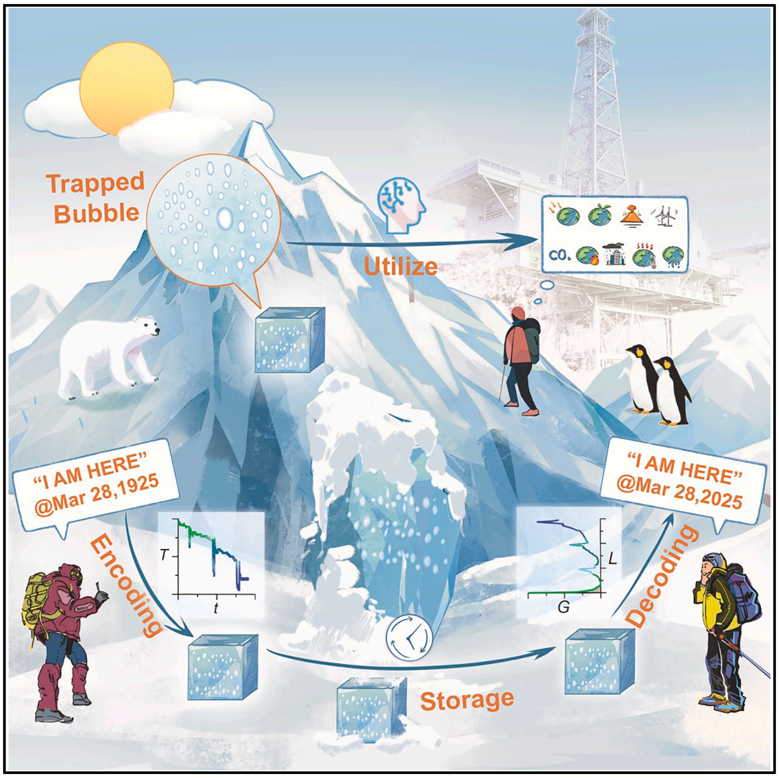

Authors

Keke Shao, Xuan Zhang,
Mengjie Song, ..., Dong Rip Kim,
Christopher Yu Hang Chao, Long Zhang

Correspondence

mengjie.song@bit.edu.cn

In brief

Shao et al. revealed the underlying physical mechanisms of the formation of trapped air bubbles and the growth of intermittent bubble layers. The bubble and clear ice regions are dependent on the freezing rate, and messages can be stored by manipulating bubble layers in ice.

Highlights

- Underlying physics of the trapped air bubble formation is analyzed
- The bubble and clear ice regions depend on freezing rate
- A sudden increase in freezing rate results in a bubble layer
- Manipulating the bubble layers to store messages in ice

Shao et al., 2025, Cell Reports Physical Science 6, 102622
June 18, 2025
https://doi.org/10.1016/j.xcrp.2025.102622

Cell Reports
Physical Science

CellPress
OPEN ACCESS

Article

Manipulating trapped air bubbles in ice for message storage in cold regions

Keke Shao,[1,10] Xuan Zhang,[1,10] Mengjie Song,[1,11,*] Jun Shen,[1] Lizhen Huang,[1] Tianzhuo Zhan,[2] Haidong Wang,[3] Bo You,[4] Libor Pekař,[5,6] Dong Rip Kim,[7] Christopher Yu Hang Chao,[8,9] and Long Zhang[1]
[1]Department of Energy and Power Engineering, School of Mechanical Engineering, Beijing Institute of Technology, Beijing 100081, China
[2]School of Mechanical Engineering & Automation, Beihang University, Beijing 100191, China
[3]Department of Engineering Mechanics, Tsinghua University, Beijing 100084, China
[4]School of Chemistry and Chemical Engineering, Huazhong University of Science and Technology, Wuhan, Hubei 430074, China
[5]Faculty of Applied Informatics, Tomas Bata University in Zlín, Nad Stráněmi 4511, 76005 Zlín, Czech Republic
[6]Department of Technical Studies, College of Polytechnics Jihlava, Tolstého 16, 58601 Jihlava, Czech Republic
[7]School of Mechanical Engineering, Hanyang University, Seoul 04763, South Korea
[8]Department of Building Environment and Energy Engineering, The Hong Kong Polytechnic University, Hong Kong 999077, China
[9]Department of Mechanical Engineering, The Hong Kong Polytechnic University, Hong Kong 999077, China
[10]These authors contributed equally
[11]Lead contact
*Correspondence: mengjie.song@bit.edu.cn

https://doi.org/10.1016/j.xcrp.2025.102622

SUMMARY

Message storage using documents and telecommunications encounters high energy consumption and a short life cycle in cold regions. Easily available low temperature and water have created the history-recording glaciers. Inspired by the naturally occurring bubbles in glaciers, we elucidate the underlying physics governing them and develop an ice-based message storage method. The formation process of trapped air bubbles is controlled by the heat and mass transfer during freezing. We identify four ice regions based on the bubbles' distribution and determine the critical freezing rate between the bubble and clear ice regions at 2.87 μm/s. Manipulating the bubble layer by varying the freezing rate successfully utilizes Morse, binary, and ternary codes to store messages. These findings reveal the underlying physics of the trapped air bubble formations, and the intermittent growth of bubble layers also provides the potential for incorporating artificial intelligence into material solidification, glacier analysis, and gas exploration.

INTRODUCTION

In the modern world, people mainly store messages in documents and telecommunications.[1,2] As our activities gradually expand to cold regions such as the poles, moon, and Mars,[3,4] the production of document- and telecommunication-based messages faces increasing challenges owing to the requirements for ink, power, and equipment,[5,6] and the long-term preservation of paper and magnetic media for storing messages also becomes difficult. Inspired by the natural air bubbles in glaciers, which record and preserve samples of air from the early history of the Earth,[7,8] we found that it is possible to store messages by manipulating trapped air bubbles in ice. This method adaptively utilizes the naturally cold environments and the abundant water and ice resources in the polar regions, and thus, no additional power is required.[9,10] The ice media can be preserved for a long time, and the trapped air bubbles, as well as their carried messages, are fully visualized and easy to read.[11] Besides, physically understanding the formation and intermittent growth mechanisms of bubbles during the water freezing process, especially with the help of artificial intelligence and machine vision, will help deepen the understanding of glacier evolution, promote the exploration of under-ice natural gas,[12] and optimize the solidification process of metal,[13,14] glass,[15] and other materials.

Gas bubbles are always trapped during the freezing of water[16,17] because of the different solubilities in liquid and solid phases. The characteristics of trapped air bubbles in ice are influenced by the type and solubility of the dissolved gas, plate temperature, ambient pressure, and freezing rate.[18,19] The increase in the initial gas concentration enlarges the trapped bubble but has very little influence on the distance between layers of bubbles.[20–22] The bubble size also increases as the freezing rate and ambient pressure go down.[23,24] The trapped air bubbles are classified into egg-shaped and needle-shaped bubbles (ESBs and NSBs, respectively) according to their aspect ratios,[24,25] and thus the bubble ice (BI) is divided into egg-shaped, egg- and needle-shaped, and needle-shaped bubble ice (ESBI, E&NSBI, and NSBI, respectively) regions. There is a greater tendency to form egg-shaped BI at a larger solubility and freezing rate.[24,26] Under a gradient temperature, the bubble shape and position may change over time.[27,28] Although some advances in understanding the features of trapped air bubbles in ice have been reported, the dividing aspect ratio for ESBs and

NSBs and the boundaries for different BI regions are still unconfirmed. Moreover, the physical aspects of the intermittent growth of trapped air bubbles and the manipulating mechanism of bubble layers (BLs) remain poorly understood, and how to apply them to message storage also needs to be explored.[26,29]

To avoid the problems faced by conventional document- and telecommunication-based methods in cold regions, we propose a potential message delivery method by manipulating trapped air bubbles in the ice. We explore the formation mechanism of a single trapped air bubble as well as its features and quantify the relationship between the BI region and the freezing rate depending on the plate temperature and freezing direction. Furthermore, we physically analyze the intermittent bubble growth to obtain the critical conditions for generating BLs. By adjusting the distribution of BLs in ice via plate temperature and recognizing them automatically by gray value, we design the procedures for manipulating BLs to fulfill message delivery and successfully deliver Arabic numerals and English letters in Morse, binary, and ternary codes. These findings will help reveal the formation mechanism of trapped air bubbles in ice and other solids, guide the design of message storage in cold regions, and advance the relevant applications of ice making, material solidification, glacier analysis, and gas exploration.

RESULTS

Formation of a trapped air bubble in ice

As shown in Figure 1A, a large number of air bubbles are trapped in a Hele-Shaw cell (Figure S1) when the water film is frozen into an ice slice (Figure 1B). A trapped air bubble in ice generally undergoes nucleation, growth, shrinking, and trapping stages (Figure 1C). When a freezing front advances, the dissolved air in the frozen water film is squeezed out because of the decrease in solubility, and it accumulates near the freezing front (Note S1). Once the air concentration exceeds a critical value, a bubble embryo nucleates at a certain point.[26] Then, the tiny bubble continuously grows, with the air near the freezing front transported to the bubble under the concentration gradient. Next, since the increasing ice length reduces the advancing speed as well as the air concentration, the bubble starts to shrink when the air transportation is slower than the bubble growth. Finally, the air bubble is closed by the freezing front and is trapped in ice. The temporal bubble size is estimated by the temporal width (W) at the freezing front and the temporal height (H), while the final bubble shape is characterized by the aspect ratio (AR) of height (H_b) to width (W_b). The above four stages are repeated for trapped air bubbles of different shapes and sizes. Normally, all the trapped air bubbles could be categorized into two shapes,[17,23] i.e., ESBs (Figure 1D) and NSBs (Figure 1E), and they differ in both shape and size changes (Figure S2; Video S1). An ESB with $AR = 2.5$ and an NSB with $AR = 10$ both increase rapidly from zero in the growth stage. Their temporal widths reach maxima at t_W and then remain, while the temporal heights keep increasing until the shrinking stage. The NSB holds a much longer growth stage than the ESB. Finally, the temporal widths reduce to zero, and the temporal heights reach maxima at t_H, generating trapped air bubbles.

In the early growth stage (before t_W), both the ESBs and NSBs are partially trapped in ice, with the upper cap staying in water. By simplifying the bubble cap as a hemisphere and balancing air transport across the air-water interface, the evolution of the bubble cap diameter, i.e., the temporal width W, can be scaled as (Note S2)

$$W \Big/ W_b \propto (t/t_W)^{1/3}, \qquad \text{(Equation 1)}$$

which is consistent with the experimental data of different ARs in Figure 1F and suggests an analogical growth law. The inset plots the normalized equivalent diameters (D/D_b, where $D = \sqrt[3]{HW^2}$ and $D_b = \sqrt[3]{H_b W_b^2}$) as a function of the normalized time (t/t_H). In the later growth stage, a bubble with a smaller AR shows a higher increasing rate in the normalized equivalent diameter because of the change in its shape.

The bubble shape and size are related to the advancing speed of the freezing front or freezing rate, which depends on the plate temperature. At a given plate temperature, ESBs and NSBs appear sequentially in ice (Video S2). The relationships between the lengths and widths of both ESBs and NSBs with their corresponding times satisfy the 1/3-power and 1/2-power laws (Figure 1F). The 1/3-power law has been explained by Equation 1. The 1/2-power law is due to the growth of the bubble length being close to the advancing freezing front, which could be estimated by

$$L \sim \sqrt{\frac{2k(T_s - T)t}{\rho\gamma}} = \sqrt{2\lambda t \mathrm{Ste}}, \qquad \text{(Equation 2)}$$

where L, $\lambda = k/\rho c_p$, and $\mathrm{Ste} = c_p(T_s - T)/\gamma$ denote ice length, thermal diffusion, and Stefan number, respectively, in which k, cp, γ, ρ, Ts, and T are ice thermal conductivity, water specific heat capacity, water solidification latent heat, water density, water solidification temperature, and plate temperature, respectively. Since $W_b \propto t_W^{1/3}$ and $H_b \propto t_H^{1/2}$, the definition of $D_b = \sqrt[3]{H_b W_b^2}$ gives $D_b \propto t_H^{5/18}$. The experimental values and mathematical model calculations of the time-dependent trends of the equivalent diameters of ESBs and NSBs at different plate temperatures are in good agreement (Figure 1H).

Effects of plate temperature and freezing direction on bubble ice regions

After counting the widths and heights (Figure 2A) as well as the AR values (Figure 2B) of all trapped air bubbles at different plate temperatures, it is found that they have the same distribution patterns, where $AR = 5$ is a critical value and can be employed to distinguish between ESBs and NSBs (Figure S3). After counting the widths and heights (Figure 2C) as well as the AR values (Figure 2D) of all trapped air bubbles at different freezing directions, it is found that they also have the same distribution patterns, where $AR = 5$ is a critical value and can be employed to distinguish between ESBs and NSBs (Figure S4).

According to the positions of ESBs and NSBs in ice, the BI is further divided into three regions, i.e., ESBI, E&NSBI, and NSBI.

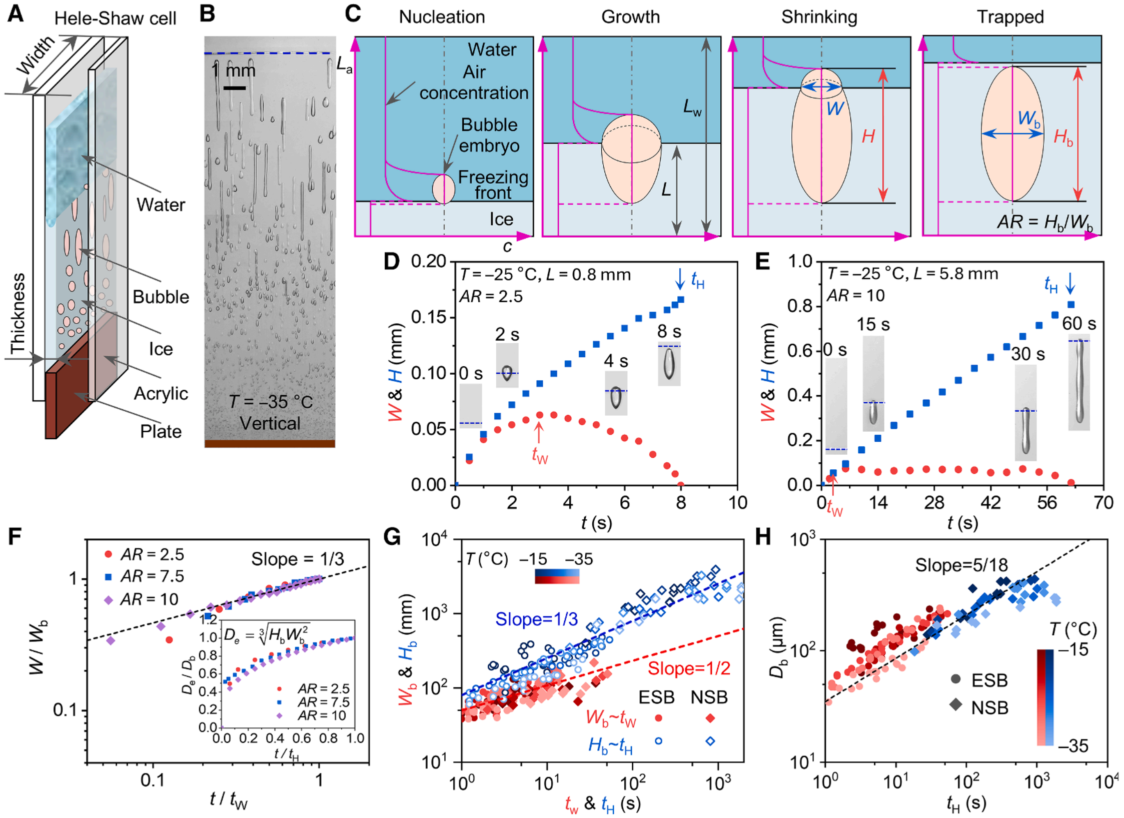

Figure 1. Formation processes and characteristics of trapped air bubbles in ice

(A) Semi-profile schematic diagram of the Hele-Shaw cell for freezing experiments.

(B) An experimental image of trapped air bubbles in ice. The dashed blue line represents the freezing front.

(C) Air concentration (c) distributions along the length (L) direction in ice, water, and bubble. The air concentration is greatest within the bubble and smaller in the ice and water. The air concentration is uniformly distributed in both ice and bubbles and shows an exponential decrease at the ice-water and air-water interfaces. The four stages of the formation process of a trapped air bubble, i.e., nucleation, growth, shrinking, and trapping, are shown. W and H are the temporal bubble width at the freezing front and temporal height, while W_b and H_b are the maximum bubble width and height, yielding temporal and maximum equivalent diameters ($D = \sqrt[3]{HW^2}$ and $D_b = \sqrt[3]{H_b W_b^2}$) and an aspect ratio ($AR$). The red lines indicate the air distribution in the ice, bubble, and water.

(D and E) Evolutions of temporal bubble width at the freezing front and temporal height during the formation processes of trapped air bubbles owing 2.5 and 10 aspect ratios (AR). The dashed blue line indicates the freezing front. t_W and t_H denote the durations reaching the maximum bubble width and height. They occur at ice lengths of 0.8 and 5.8 mm at a freezing temperature of −25°C.

(F) Changes of the normalized temporal bubble widths (W/W_b) with the normalized time (t/t_W) during the formation processes of AR = 2.5, 7.5, and 10 bubbles in the early growth stage, suggesting a 1/3-scaling law between them. The inset plots the normalized equivalent diameters (D_e/D_b) as a function of the normalized time (t/t_H).

(G) Changes in width and height dimensions of ESBs and NSBs with the corresponding times.

(H) Plot of equivalent bubble diameter (D_b) as a function of the maximum bubble height time (t_H).

Decreasing the plate temperature and increasing the freezing direction (θ, defined as the inclination angle between the cell plane and the direction opposite to gravity) both diminish the sizes of the ESBs and NSBs (Figures 2D and 2E) and elongate the ESBI, E&NSBI, and NSBI regions (Figures S5 and S6) owing to a higher freezing rate at the same position. However, they hardly influence the critical aspect ratios distinguishing ESBs and NSBs.

Manipulation of intermittent bubble growth and bubble layers in ice

To simply calculate the freezing rate of water film in a Hele-Shaw cell at different directions, the heat convection in the water film and near the outside surface of the cell is considered by two additional empirical relations for temperature and heat transfer coefficient depending on the freezing direction. Thus, Equation 3 is further modified as

$$\gamma\rho\frac{dL}{dt} = k\frac{T_s - T}{L} - h_w(T_w - T_s) - h_a\frac{2L}{D_c}(T_a - T_c),$$

(Equation 3)

where D_c is the cell thickness, T_a and $T_w = T_a(0.75 + 0.25\cos\theta)$ are the air temperature and the average temperature of the water film during freezing, $T_c = (T_s + T)/2$ is the average temperature of the side surface of the cell, $h_w = 240 - 20\cos\theta$ and

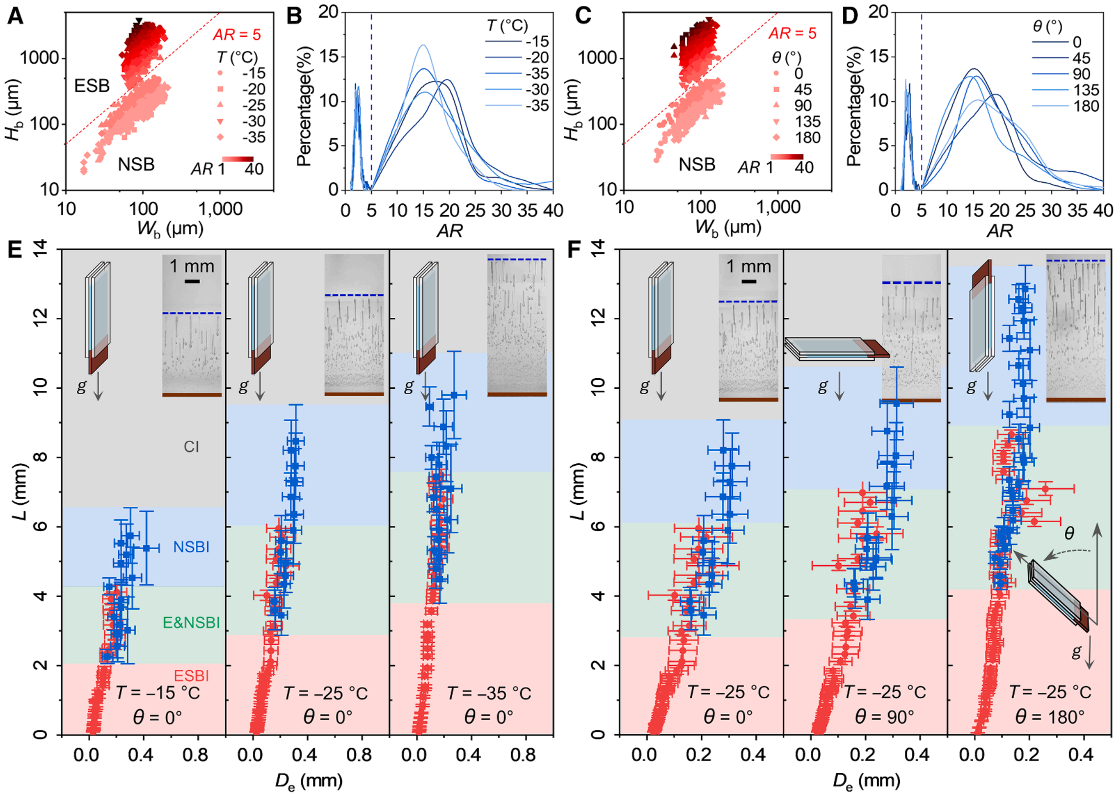

Figure 2. Effects of plate temperature and freezing direction on bubble ice regions

(A) Trapped air bubble widths and heights at different plate temperatures.

(B) Percentages of bubble aspect ratios at different plate temperatures, dividing the trapped air bubbles into two types, egg-shaped ($AR \leq 5$) and needle-shaped ($AR > 5$) bubbles (ESBs and NSBs, respectively).

(C) Trapped air bubble widths and heights at different freezing directions.

(D) Percentages of bubble aspect ratios at different freezing directions, dividing the trapped air bubbles into two types, ESBs ($AR \leq 5$) and NSBs ($AR > 5$).

(E and F) Equivalent bubble diameters (D_e) along the ice length (L) at various plate temperatures (T) and freezing directions (θ). According to the positions of ESBs and NSBs in ice, the bubble ice region can be further divided into egg-shaped (red), egg- and needle-shaped (green), and needle-shaped (blue) bubble ice (ESBI, E&NSBI, and NSBI, respectively). A region without bubbles (black) is called clear ice (CI). For each data point, the vertical and horizontal caps represent the height and 5× the width of the trapped air bubble.

$h_a = 0.5 - 0.1\cos\theta$ are the heat transfer coefficients between ice and water at the freezing front and between the cell and air, which are both related to the freezing direction (Note S3). A comparison with the experimental results demonstrates that Equation 3 could predict the temporal ice height at different plate temperatures (Figure 3A; Video S3) and freezing directions (Figure 3B; Video S4). The freezing rate reduces as the freezing front advances owing to the larger thermal resistance. A higher plate temperature or smaller inclination angle reduces the driving force or enhances the heat exchange between the cell and the surrounding air and thus slows down the freezing, yielding a shorter ice slice at the same time. In addition, Hele-Shaw cell thickness also affects the freezing rate, which decreases as the thickness increases.

As the freezing rate reduces, the trapped air bubbles change from ESBs and NSBs and finally disappear, forming ESBI, E&NSBI, NSBI, and clear ice (CI) regions in sequence (Video S2). The map of ESBI, E&NSBI, NSBI, and CI regions indicates that the critical freezing rates are almost the same for different bubble region boundaries at different plate temperatures and freezing directions (Figure 3C). The critical freezing rates for the ESBI-E&NSBI, E&NSBI-NSBI, and NSBI-CI boundaries are 20.05 ± 0.91, 9.90 ± 0.47, and 2.87 ± 0.28 μm/s, respectively.

Since the type of BI region is determined by the freezing rate, it becomes possible to manually control the freezing rate to manipulate the bubble shape and distribution in ice. Two easy control strategies are tested, i.e., temperature-constant (Figure 3D) and rate-constant (Figure 3E). In the temperature-constant strategy, the plate temperature is fixed at $-15°C$, and the freezing rate gradually decreases, which could be predicted by Equation 3. In the rate-constant strategy, the plate temperature is continuously reduced to control the freezing rate at around 15 μm/s, where E&NSBI appears. The evolution of the plate temperature can also be obtained from Equation 3. Similarly, for any expected freezing rate in the manipulation of BI, Equation 3 is capable of calculating the temporal plate temperature control curve (Figure 3F).

When controlling the freezing rate alternately below or above the critical value for the NSBI-CI boundary by adjusting the plate temperature in real time (Figure 4A) and intermittently adjusting

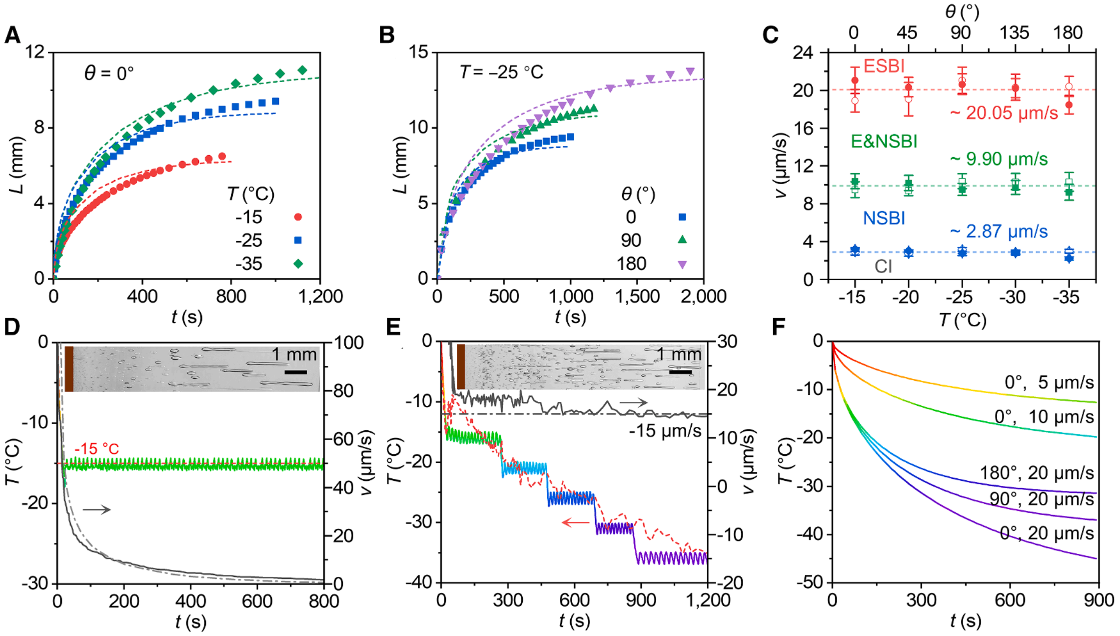

Figure 3. Freezing characteristics at various plate temperatures and freezing directions

(A and B) Evolution of ice lengths at various plate temperatures and freezing directions. The dashed lines are predicted by the theoretical model.

(C) A regime map of ESBI, E&NSBI, NSBI, and CI regions in terms of the freezing rate (v), the plate temperature, and freezing direction. The critical freezing rate for the emergence of bubbles in ice is about $v_{\text{NSBI-CI}}$ = 2.87 μm/s. Error bars are the standard deviation of the experimental results, with solid and hollow points corresponding to plate temperature and freezing direction, respectively.

(D and E) Evolution of plate temperatures and freezing rates under temperature-constant and rate-constant control strategies in experiments. The insets are the experimental images of bubble ice.

(F) Evolution of plate temperatures calculated from the theoretical model for five different groups of freezing rates and directions.

the bubble growth, alternate layers of BI and CI will be generated (Figure 4B). Thus, the size and position of trapped air bubbles can be regulated by changing the plate temperature during freezing. Each sharp decrease in the plate temperature results in a sudden climb of the freezing rate, yielding a single BL. Therefore, the trough on each temperature control curve (Figure 4A) has the same number as the BL in the corresponding ice image (Figure 4B). In addition, as can be seen in Figure 4B, some undesired bubbles appeared in the CI region due to invisible impurities in the water. These bubbles do not interfere with the identification of the BL (Figure S7).

During the formation process of the j_{th} BL (Figure 5A), the plate temperature dramatically decreases from $T_{j-0.5}$ to T_j and then increases to $T_{j+0.5}$ with the freezing rate increasing from $v_{j-0.5}$ to v_j and then decreasing to $v_{j+0.5}$. The BL starts at $L_{j-0.5}$ and ends at $L_{j-0.5}$ with a center position of L_j. To speed up the freezing process, the freezing rates before and after each BL are controlled just below the critical freezing rate for the NSBI-CI boundary ($v_{\text{NSBI-CI}}$), i.e., $v_{j-0.5} = v_{j+0.5} \approx 3$ μm/s. In addition, further studies revealed that the response time of the BL is in the order of seconds and proportional to the quadratic of the ice length (Note S4). All the BLs in Figure 4B are above the 1.5 mm position, and the stable control requires a minimum BL height ($L_{j+0.5} - L_{j-0.5}$) of 1.5 mm (Figure 5B). For accurate control, each BL height is fixed at 1.5 mm, with the first 1.5 mm of the ice serving as the initial region (IR). As the ice length increases, the freezing rate increase ($v_j - v_{j-0.5}$) required for the formation of the BL shows a gradually decreasing trend (Figure 5C). To ensure the successful formation of all five BLs, the freezing rate increase should be over 10.6 μm/s.

Using the minimum BL height and freezing rate increase as the critical parameters in manipulating BLs in ice, both the temporal plate temperature and freezing rate curves during the formation processes of the fifth BL (Figure 5D) and all three BLs (Figure 5E) are predicted by Equation 3, achieving good agreement with the experimental data. For the first four BLs, which are more easily realized (Figure 5D), comparisons of the plate temperature and freezing rate curves between the experiment and theoretical model are provided in Figure S8.

Message delivery by bubble layers in ice

The gray value extracted from the ice image containing BLs could be easily read by a computer. It is also possible to manipulate the formation of BLs in ice by adjusting the plate temperature according to the input message. Thus, messages can be delivered by encoding trapped air bubbles in ice with the seven main procedures illustrated in Figure 6A, including input, transformation, encoding, acquisition, decoding, operation, and output. First, messages are input into the system via external devices based on user requirements. Second, the input messages are transformed into temperature control signals. Third, the temperature control curve adjusts the distribution and shape of the trapped air bubbles in real time, and thus an ice slice containing BLs is encoded in a Hele-Shaw cell, which is the most important step in the message delivery.

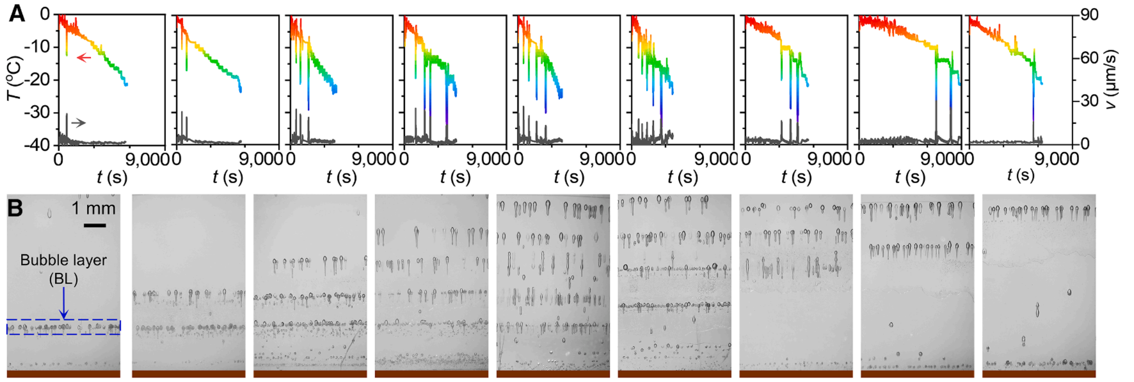

Figure 4. Experimental plate temperature control curves and the corresponding images

(A) Ten sets of plate temperature (*T*) control curves and freezing rate curves for intermittent bubble growth and manipulating bubble layers (BLs) in ice.

(B) Ten experimental images of ice containing BLs corresponding to (A). Each sharp decrease in the plate temperature (*T*) results in a sudden climb in the freezing rate (*v*), yielding a single BL. Therefore, the trough on each temperature control curve in (A) has the same number as the BL in the corresponding ice image.

Fourth, an optical image of the encoded ice is acquired by a camera. Fifth, the normalized average gray value of the acquired images along the ice height (Note S5) is automatically calculated, and hence, the position and number of BLs are decoded. Sixth, an operation is performed to convert the rough position and number on the gray value curve into digital data, which are quite distinct for different operators, such as Morse, binary, and ternary codes. Seventh, the data are output as readable messages.

Defining the BI and CI layers as “dah” and “dit” in Morse code (Table S1), Figure 6B presents the temperature control curve, encoded ice image, and decoded gray value curve for encoding Arabic numeral 1. Each arrow next to the temperature control curve indicates a sharp decrease in plate temperature, i.e., a trough, causing a BI layer in the encoded ice image. Each image is divided into one IR and five equal-length encoding regions (ERs) with the normalized gray value curve inserted. Each trough of the gray value curve caused by the BI layer denotes a dah. Thus, a message can be transferred to the temperature control curve and read from the resulting ice image, completing the whole delivery process perfectly. When delivering 26 letters of the English alphabet, it is sufficient to employ only some of the five ERs for a faster delivery speed. For example, when encoding the English letter A (Figure 6C), the freezing front in the ice image produces a peak in the gray value curve, which serves as a terminator to end the encoding and decoding steps in a timely manner. The encoding results of all 26 letters of the English alphabet are available in Figure S9.

Regarding the BI and CI layers as 1 and 0 in Binary code, it is necessary to encode the Arabic numeral 11 (Figure 6D), and the encoding results of all 32 Arabic numerals are provided in Figure S10 and Video S5. Furthermore, if the NSBI, ESBI, and CI layers represent 2, 1, and 0 in ternary code, respectively, the Arabic numeral 19 and more messages could be delivered (Figure 6E; Video S6). Generally, the NSBI and ESBI layers could be distinguished by the ratio of the rough width on the gray value curve to the ER height.

To evaluate the performance of different operators, Figures 7A and 7B plot maps of four indicators, i.e., temperature curve controllability, BL controllability, gray value recognizability, and encoding time, for 10 Arabic numerals and 26 English letters in Morse code and 32 Arabic numerals in binary code, with all the values normalized. For a standard comparison, the values of all the indicators are normalized to control them between 0 and 1. The values of the encoding time, BL controllability, and temperature curve controllability are normalized by

$$\bar{M} = \frac{M_{\max} - M}{M_{\max} - M_{\min}}. \qquad \text{(Equation 4)}$$

The value of the gray curve recognizability’s is normalized by

$$\bar{M}_R = \frac{M_R - M_{R,\min}}{M_{R,\max} - M_{R,\min}}. \qquad \text{(Equation 5)}$$

The definitions and calculations of all indicators are given in Note S6. Combining the four indicators, E and I in Morse code and 5, 12, 17, and 21 in binary code are the top choices for effective message delivery. The seven steps of the delivery processes for the English letters A and E by Morse code and the Arabic numeral 5 by binary code are provided in Video S7.

Furthermore, Figure 7C compares the capacities of Morse, binary, and ternary codes for message delivery. The message capacity determines the maximum number of messages that can be communicated by a code system. Generally, the message capacity of a code system without a terminator could be calculated by

$$C_m = P^n, \qquad \text{(Equation 6)}$$

where P is the digit corresponding to the code system and n is the number of ERs. For the binary and ternary codes, $P = 2$ and 3, respectively. When a terminator is introduced, the Morse code can cover 26 English letters. The message capacity of a Morse code system becomes

$$C_m = \sum_{i=1}^{n} P^i. \qquad \text{(Equation 7)}$$

When introducing a terminator, the message capacities of all three codes almost double. The ternary and binary codes have

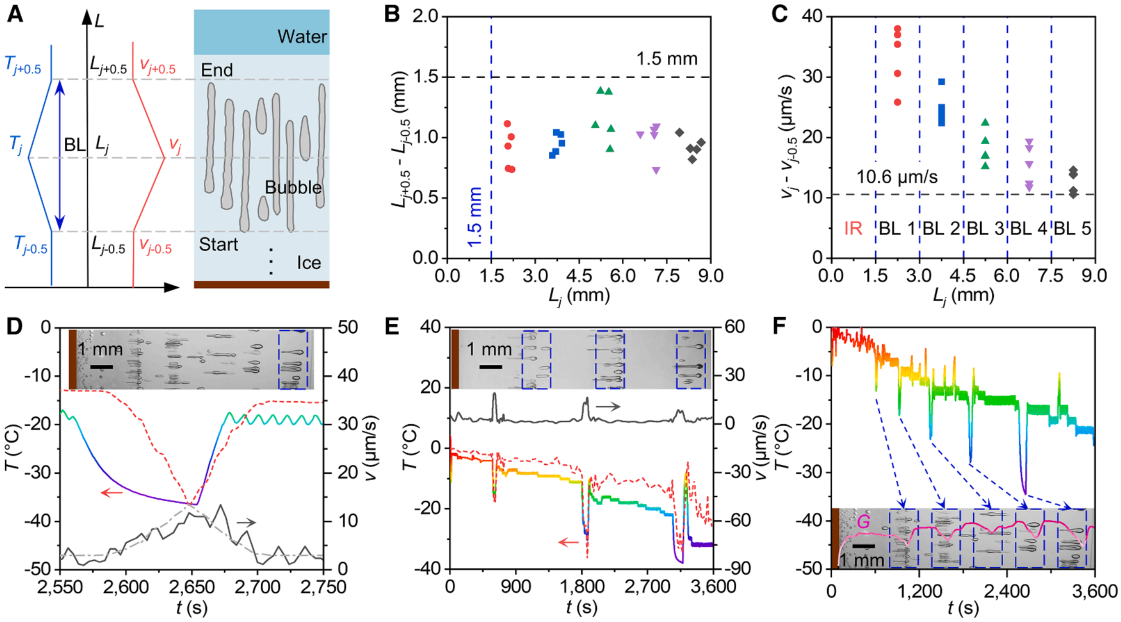

Figure 5. Principles of manipulation of bubble layers in ice

(A) Schematic diagram of plate temperature and freezing rate changes during the formation process of a bubble layer (BL) in ice. To speed up the formation process, the freezing rates before and after each BL are controlled just below the critical freezing rate for the NSBI-CI boundary ($v_{NSBI-CI}$), i.e., $v_{j-0.5} = v_{j+0.5} \approx$ 2.8 μm/s.

(B) Plot of the BL height ($L_{j+0.5} - L_{j-0.5}$) as a function of the BL center position (L_j). All the BLs in (B) are above 1.5 mm position, and the stable control requires a minimum BL height of 1.5 mm.

(C) Plot of the freezing rate increase ($v_j - v_{j-0.5}$) during the formation of BLs as a function of the BL center position. For accurate control, each BL height is fixed at 1.5 mm, with the first 1.5 mm of ice serving as the initial region (IR). To ensure the successful formation of all five BLs, the freezing rate increase should be over 10.6 μm/s.

(D and E) Comparisons of the temporal plate temperature and freezing rate curves during the formation processes of the fifth BL and all three BLs between the experiments and theoretical equation.

(F) Plate temperature curve for five BLs and normalized average gray value (G) along the ice length. Each BL caused by a sharp decrease in the plate temperature reduces the local gray value and hence forms a trough, which could be used for the automatic recognition of the BL.

10.1 and 1.7 times the capacities of the Morse code, respectively. Considering the message capacity, the Morse and binary codes are further compared comprehensively in Figures 7D and S11, Table S2, and Note S6. In addition, the message storage capacity can be significantly increased by varying the size of the coding regions (Note S7). Due to the fact that trinary encoding is more difficult to control, there is not enough data to compare it with the other two encoding methods.

The Morse code has an advantage in the temperature curve controllability, but the binary code is recommended overall. It can be expected that the message capacity will go up exponentially (Figure S12) when multiple cells are used. Two Morse code-based cells controlled by cooling systems were also tested successfully for the delivery of the English letters FL (Figure 7E), CN, and BJ (Figure S13; Video S8).

DISCUSSION

The findings here elucidate the underlying physics governing and manipulating the formation of trapped air bubbles and intermittent growth of bubble layers in ice and other solids. The message storage method of manipulating trapped air bubbles in ice utilizes easily available low-temperature and water resources in cold regions and overcomes the challenges of a short life cycle and the requirements for additional equipment and media encountered by the conventional document- and telecommunication-based methods. In cold regions, the use of trapped air bubbles as a means of message delivery and storage requires less energy than telecommunication and is more covert than documents. In particular, trapped air bubbles in ice are advantageous for message storage (Note S8). Furthermore, although encoding per character consumes more energy when the entire time it takes to deliver the message is taken into account, the average energy consumption for message delivery becomes lower. In addition, although changes such as deformation and migration of trapped air bubbles in ice may occur after long periods,[30,31] these changes do not affect the efficiency of message delivery and storage when ice is preserved in polar regions in environments with small temperature gradients.

In the future, the growth dynamics of a single trapped air bubble, the effects of gas type and ambient pressure on the bubble ice characteristics, the control of more bubble layers and Hele-Shaw cells, and the thermal stability[28,32] of trapped air bubbles demand further investigation. Furthermore, while this work utilizes the changes in gray value caused by the trapped bubbles to develop a new message delivery method, the trapped air

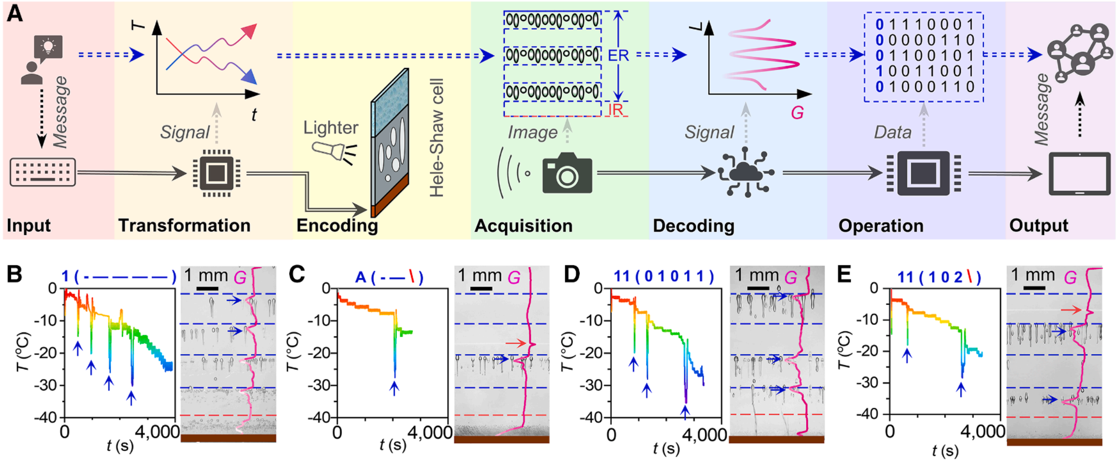

Figure 6. Message delivery by encoding bubble layers in ice

(A) Schematic diagram of the seven steps of the message delivery process by encoding trapped air bubbles in ice.

(B) Temperature control curve, encoded ice image, and decoded gray value curve for encoding Arabic numeral 1 with the bubble and clear ice (BI and CI) layers representing dah and dit in Morse code. Each arrow next to the temperature control curve indicates a sharp decrease in plate temperature, i.e., a trough, causing a BI layer in the encoded ice image. The image is divided into one initial region (IR) and five encoding regions (ERs), with the normalized gray value curve inserted. Each trough of the gray value curve caused by the BI layer denotes a dah. Thus, a message can be delivered by the temperature control curve and read from the ice image.

(C) Temperature control curve, encoded ice image, and decoded gray value curve for encoding English letter A in Morse code. The freezing front in the ice image produces a peak in the gray value curve and denotes a terminator in Morse code.

(D) Temperature control curve, encoded ice image, and decoded gray value for encoding Arabic numeral 11, with the BI and CI layers representing 1 and 0 in binary code.

(E) Temperature control curve, encoded ice image, and decoded gray value curve for encoding Arabic numeral 19, with the NSBI, ESBI, and CI layers representing 2, 1, and 0 in ternary code.

bubbles also significantly adjust the optical transparency[33,34] (Figure S14) of ice and reduce its mechanical compressive strength[35] because of the stress concentration (Figure S15). Studies have shown that air bubbles in glaciers change their melting rate and thus the climate.[36,37] A combination of artificial intelligence and machine vision also provides the possibility to acquire more digital characteristics of trapped bubbles in ice and glaciers. The study of the growth and distribution characteristics of trapped air bubbles in ice can provide a reference for metal smelting.[38,39] Meanwhile, air bubbles in ice can store gases such as ozone, which can be used for preserving food such as seafood.[40,41] In addition, trapped air bubbles are also expected to be useful in the field of biopharmaceuticals as containers for slow-release drugs.

In summary, we develop a message delivery method by manipulating trapped air bubbles in ice and solve the underlying fundamental and technical problems. First, we reveal the formation mechanism of a single trapped bubble in ice. Owing to the difference in solubility, air bubbles are trapped when the water film is frozen into an ice slice and undergoes nucleation, growth, shrinking, and trapping stages. Defining the aspect ratio of bubble height to width, we categorize all the bubbles into egg-shaped bubbles and needle-shaped bubbles by an aspect ratio of five. Then, we identify the egg-shaped, egg- and needle-shaped, needle-shaped, and clear ice regions based on the distinct distributions of bubbles. Surprisingly, the boundaries between the four ice regions depend on the freezing rates, which are ~20.05, ~9.90, and ~2.87 μm/s, respectively. We also establish a theoretical model to predict the freezing rate under various plate temperatures and freezing directions. Next, we control the distribution of trapped air bubbles by adjusting the temporal freezing rate. Interestingly, a sudden climb in the freezing rate caused by a sharp decrease in the plate temperature results in a single bubble layer. The minimum bubble layer height and the freezing rate increase are determined to be 1.5 mm and 10.6 μm/s, respectively. Using these two values as the critical parameters in the theoretical model, we further achieve the manipulation of bubble layers in ice by controlling the plate temperature and the automatic recognition of them via gray value. Finally, we propose the seven procedures for manipulating bubble layers to fulfill message delivery and successfully deliver Arabic numerals and English letters by regarding the bubble and clear ice layers as different signals in Morse, binary, and ternary codes. We comprehensively compare the Morse and binary codes in terms of temperature curve controllability, bubble layer controllability, gray value recognizability, encoding time, and message capacity and recommend the binary code for more achievable message delivery.

METHODS

Preparations of water samples and Hele-Shaw cells

To ensure that the water is saturated with dissolved air, all the water samples (deionized water, CAS#7732-18-5, Aladdin) are placed in a beaker and left in a clean room (20°C ± 1°C) for 24 h

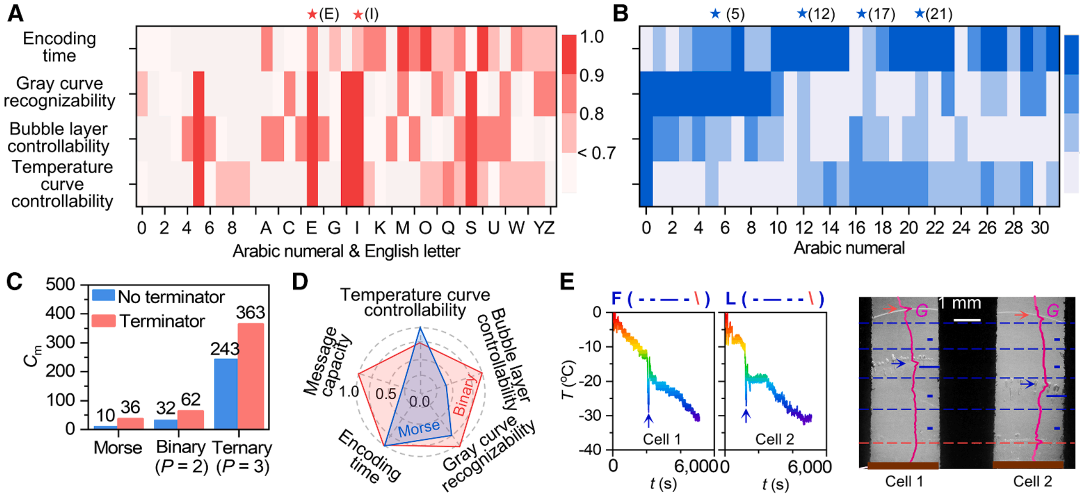

Figure 7. Comparison of different encoding methods

(A and B) Maps of temperature curve controllability encoding time, bubble layer controllability, and gray value recognizability for 10 Arabic numerals and 26 English letters in Morse code and 32 Arabic numerals in binary code. Combining the four indicators, E and I in Morse code and 5, 12, 17, and 21 in binary code are top choices for effective message delivery.

(C) Message capacities of Morse, binary, and ternary codes with and without a terminator.

(D) A radar map for a comprehensive comparison between Morse and binary codes in terms of temperature curve controllability, bubble layer controllability, gray value recognizability, encoding time, and message capacity. The binary code is recommended overall.

(E) Temperature control curves, encoded ice images, and decoded gray value curves for encoding the English letters F and L using two Morse code-based cells. The two cells are linked to two separate refrigeration systems to control the plate temperature independently.

before being used. Each Hele-Shaw cell for water freezing comprises two acrylic plates and a copper plate serving as a plate (Figure S1). Each acrylic plate has a dimension of 50 mm height × 50 mm width × 5 mm thickness. The acrylic plate and the cooper plate show contact angles of 64.4° ± 3.2° and 72.6° ± 4.5°, respectively, measured at 20°C ± 1°C (Figure S1C). The copper plate has a dimension of 50 mm height × 40 mm width × 0.5 mm thickness (Figure S1D). To eliminate the effects of impurities, all the acrylic plates and cooper plates are washed with ethanol (CAS#64-17-5, Aladdin) and deionized water for 5 min. Then, the former and the latter are put into a vacuum drying oven at 50°C and 80°C for 1 h.

Experimental setup for the freezing of water film

The experimental setup for the freezing of water film (Figure S16) consists of a plate temperature control system, a data acquisition system, an image acquisition system, and a Hele-Shaw cell. The plate temperature control system includes a programmable DC power supply (RIGOL DP811A, 0.05% accuracy for voltage regulation), a semiconductor plate (TEC2-19006), a heat exchanger, and a constant-temperature water bath. The data acquisition system includes six T-type thermocouples (0.2°C accuracy), a temperature and humidity sensor (Rotronic HF532, 0.1°C accuracy for temperature and 0.8% accuracy for humidity), and a data acquisition unit (Agilent 34970A). The image acquisition contains a cold light, a CCD camera (AOSVI 3M50 with a 4.5× lens), and a diffuser. The above three systems are all connected to a computer for data storage. To avoid condensation and frosting, the Hele-Shaw cell is covered with a protective chamber, where 99.999% pure nitrogen (N_2, CAS#7727-37-9, Beijing Haipu Beifen Qiti Ind.) is slowly fed during experiments.

Experimental details

All experiments are conducted in a closed dark room at 20°C ± 1°C room temperature and 30% ± 3% relative humidity. In experiments, deionized water is injected into the Hele-Shaw cell in advance. By adjusting the input voltage of the semiconductor plate, the plate temperature can be controlled. Here, the plate temperature ranges from -15°C to -35°C with a 5°C internal temperature. The freezing direction or the inclination angle of the Hele-Shaw cell is adjusted from 0° to 180°, with a 45° internal temperature. Since the set plate temperature is well below the freezing point of deionized water, the water film may start to freeze before the plate temperature reaches the set value. However, the cooling stage occupies less than 6% of the total time in each freezing experiment (Figure S17), and thus it is reasonable to ignore the influence of the cooling stage on the experimental results.

The seven steps of the delivery processes of the English letters and the Arabic numerals by Morse, binary, and ternary codes are completed with the help of LabVIEW software. Self-developed MATLAB codes are used to transform the message into the control voltage curve for the semiconductor plate in the transformation step, calculate the image gray value in the decoding step, and convert the rough position and number on the gray value curve into digital data in the operation step.

Data processing

During the water freezing experiments, the camera is set to record videos at a speed of 10 fps and a resolution of 1.5 μm/pixel.

All the experimental data, such as ice length, bubble width, bubble length, and bubble position, are quantitatively extracted from the video-exported images with the help of ImageJ software.

RESOURCE AVAILABILITY

Lead contact

Further information and requests for resources and reagents should be directed to and will be fulfilled by the lead contact, Mengjie Song (mengjie.song@bit.edu.cn).

Materials availability

This study did not generate new unique materials.

Data and code availability

- All data reported in this paper will be made available by the lead contact upon request.
- This paper does not report original code.
- Any additional information required to reanalyze the data reported in this paper is available from the lead contact upon request.

ACKNOWLEDGMENTS

This work is supported by the National Natural Science Foundation of China (nos. 52076013, 52406007, and 52306003); Beijing Municipal Commission of Science and Technology, Zhongguancun Science and Technology Park Management Committee (nos. 3212024, 3244046, 3232032, and Z231100006123010); Department of Science and Technology of Hebei Province (no. 244A7625D); China Postdoctoral Science Foundation (no. 2022M720423); Key Laboratory of Icing and Anti/De-icing (nos. IADL20230113 and IADL20220304); and Young Elite Scientist Sponsorship Program by BAST (no. BYESS2023352).

AUTHOR CONTRIBUTIONS

K.S. and X.Z. contributed equally to this work. K.S., X.Z., and M.S. conceived the idea for the work. K.S., X.Z., and L.H. performed the experiments. M.S., J. S., T.Z., H.W., B.Y., L.P., D.R.K., and C.Y.H.C. guided the experiments. K.S. and X.Z. developed the theoretical models and analyzed the data. X.Z. performed the simulations. K.S. and X.Z. wrote the manuscript. M.S., H.W., B. Y., and T.Z. edited the manuscript. M.S., J.S., and L.Z. supervised the work. All authors have approved the final version of the manuscript.

DECLARATION OF INTERESTS

The authors declare no competing interests.

SUPPLEMENTAL INFORMATION

Supplemental information can be found online at https://doi.org/10.1016/j.xcrp.2025.102622.

Received: December 20, 2024
Revised: March 28, 2025
Accepted: May 13, 2025

REFERENCES

1. Whillans, I.M. (1976). Radio-echo layers and the recent stability of the West Antarctic ice sheet. Nature *264*, 152–155. https://doi.org/10.1038/264152a0.
2. Wannamaker, P.E., Stodt, J.A., Pellerin, L., Olsen, S.L., and Hall, D.B. (2004). Structure and thermal regime beneath the South Pole region, East Antarctica, from magnetotelluric measurements. Geophys. J. Int. *157*, 36–54. https://doi.org/10.1111/j.1365-246X.2004.02156.x.
3. Martellosio, A., Pasian, M., Perregrini, L., Piffer, L., Riccardi, R., Concaro, F., and Besso, P. (2017). High-frequency radomes for polar region ground stations: the state of the art and novel developments of radome technologies. IEEE Antennas Propag. Mag. *59*, 88–101. https://doi.org/10.1109/MAP.2017.2752694.
4. Baker, V.R. (2001). Water and the Martian landscape. Nature *412*, 228–236. https://doi.org/10.1038/35084172.
5. Menaka, D., Gauni, S., Manimegalai, C.T., and Kalimuthu, K. (2022). Challenges and vision of wireless optical and acoustic communication in underwater environment. Int. J. Commun. Syst. *35*, e5227. https://doi.org/10.1002/dac.5227.
6. Washburn, A.L. (1980). Focus on polar research. Science *209*, 643–652. https://doi.org/10.1126/science.209.4457.643.
7. Yan, Y., Brook, E.J., Kurbatov, A.V., Severinghaus, J.P., and Higgins, J.A. (2021). Ice core evidence for atmospheric oxygen decline since the Mid-Pleistocene transition. Sci. Adv. *7*, eabj9341. https://doi.org/10.1126/sciadv.abj9341.
8. Alley, R.B. (2000). Ice-core evidence of abrupt climate changes. P. Natl. Acad. Sci. USA *97*, 1331–1334. https://doi.org/10.1073/pnas.97.4.1331.
9. Chang, T., Moses, O.A., Tian, C., Wang, H., Song, L., and Zhao, G. (2021). Synergistic ice inhibition effect enhances rapid freezing cryopreservation with low concentration of cryoprotectants. Adv. Sci. *8*, 2003387. https://doi.org/10.1002/advs.202003387.
10. Garg, A., Yerneni, S.S., Campbell, P., LeDuc, P.R., and Ozdoganlar, O.B. (2022). Freeform 3D Ice Printing (3D-ICE) at the Micro Scale. Adv. Sci. *9*, 2201566. https://doi.org/10.1002/advs.202201566.
11. Meijer, J.G., Rocha, D., Linnenbank, A.M., Diddens, C., and Lohse, D. (2024). Enhanced bubble growth near an advancing solidification front. J. Fluid Mech. *996*, A22. https://doi.org/10.1017/jfm.2024.777.
12. Wang, L., Du, Z., Wei, Z., Ouyang, W., Maher, D.T., Xu, Q., and Xiao, C. (2023). Large methane emission during ice-melt in spring from thermokarst lakes and ponds in the interior Tibetan Plateau. Catena *232*, 107454. https://doi.org/10.1016/j.catena.2023.107454.
13. Kim, C.K., Cho, D.W., Kim, S., Song, S.W., Seo, K.M., and Cho, Y.T. (2023). High-throughput metal 3D printing pen enabled by a continuous molten droplet transfer. Adv. Sci. *10*, 2205085. https://doi.org/10.1002/advs.202205085.
14. Jin, P., Yan, X., Hoque, M.J., Rabbi, K.F., Sett, S., Ma, J., Li, J., Fang, X., Carpenter, J., Cai, S., et al. (2022). Ultra-low ice-substrate adhesion and self-deicing during droplet impact freezing. Cell Rep. Phys. Sci. *3*, 100894. https://doi.org/10.1016/j.xcrp.2022.100894.
15. Peitl, O., Zanotto, E.D., and Heide, K. (2020). Crystallization-triggered bubbles in glass-ceramics. Ceram. Int. *46*, 22513–22520. https://doi.org/10.1016/j.ceramint.2020.06.011.
16. Jiang, Y., Zhao, Y., Zhang, H., Yang, C., and Cheng, P. (2024). Three-dimensional shaping strategy via solidifying polygonal nanofluid drops. Cell Rep. Phys. Sci. *5*, 101904. https://doi.org/10.1016/j.xcrp.2024.101904.
17. Shao, K., Song, M., Zhang, X., and Zhang, L. (2023). Growth and distribution characteristics of trapped air bubbles in ice slices. Phys. Fluids *35*, 113319. https://doi.org/10.1063/5.0175106.
18. Thiévenaz, V., Meijer, J.G., Lohse, D., and Sauret, A. (2024). On the shape of air bubbles trapped in ice. Proc. Natl. Acad. Sci. USA *122910*, e2415027122. https://doi.org/10.1073/pnas.2415027122.
19. Azuma, N., Miyakoshi, T., Yokoyama, S., and Takata, M. (2012). Impeding effect of air bubbles on normal grain growth of ice. J. Struct. Geol. *42*, 184–193. https://doi.org/10.1016/j.jsg.2012.05.005.
20. Murakami, K., and Nakajima, H. (2002). Formation of pores during unidirectional solidification of water containing carbon dioxide. Mater. Trans. *43*, 2582–2588. https://doi.org/10.2320/matertrans.43.2582.
21. Bari, S.A., and Hallett, J. (1974). Nucleation and growth of bubbles at an ice-water interface. J. Glaciol. *13*, 489–520. https://doi.org/10.3189/S0022143000023248.

22. Matsumoto, K., Sameshima, K., Teraoka, Y., Furuya, K., Murahashi, K., Hayashi, K., and Shirai, D. (2013). Formation of ozone ice by freezing water containing ozone micro-bubbles (Investigation into the influence of surfactant on characteristics of ice containing oxygen micro-bubbles). Int. J. Refrig. *36*, 842–851. https://doi.org/10.1016/j.ijrefrig.2012.10.030.
23. Carte, A.E. (1961). Air bubbles in ice. Proc. Phys. Soc. *77*, 757–768. https://doi.org/10.1088/0370-1328/77/3/327.
24. Yoshimura, K., Inada, T., and Koyama, S. (2008). Growth of spherical and cylindrical oxygen bubbles at an ice-water interface. Cryst. Growth Des. *8*, 2108–2115. https://doi.org/10.1021/cg070251k.
25. Inada, T., Hatakeyama, T., and Takemura, F. (2009). Gas-storage ice grown from water containing microbubbles. Int. J. Refrig. *32*, 462–471. https://doi.org/10.1016/j.ijrefrig.2008.08.008.
26. Shao, K., Song, M., Shen, J., Zhang, X., and Pekař, L. (2024). Experimental study on the distribution and growth characteristics of trapped air bubbles in ice slices at different freezing temperatures. Appl. Therm. Eng. *244*, 122600. https://doi.org/10.1016/j.applthermaleng.2024.122600.
27. Huber, C., Leuenberger, M., and Zumbrunnen, O. (2003). Continuous extraction of trapped air from bubble ice or water for on-line determination of isotope ratios. Anal. Chem. *75*, 2324–2332. https://doi.org/10.1021/ac0263972.
28. Dadic, R., Schneebeli, M., Wiese, M., Bertler, N.A.N., Salamatin, A.N., Theile, T.C., Alley, R.B., and Lipenkov, V.Y. (2019). Temperature-driven bubble migration as proxy for internal bubble pressures and bubble trapping function in ice cores. JGR. Atmospheres *124*, 10264–10282. https://doi.org/10.1029/2019JD030891.
29. Bianchi, M.V.A., and Viskanta, R. (1997). Gas segregation during solidification processes. Int. J. Heat Mass Transf. *40*, 2035–2043. https://doi.org/10.1016/S0017-9310(96)00283-9.
30. Maeno, N. (1967). Air bubble formation in ice crystals. Phys. Snow Ice: SAVE Proc. *1*, 207–218. http://eprints.lib.hokudai.ac.jp/dspace/bitstream/2115/20297/1/1.
31. Selva, B., Cantat, I., and Jullien, M.C. (2011). Temperature-induced migration of a bubble in a soft microcavity. Phys. Fluids *23*, 052002. https://doi.org/10.1063/1.3590743.
32. Shao, K., Song, M., Zhang, X., Xu, C., Wang, Y., Hu, Y., and Wang, Z. (2024). Mechanical analysis of the critical conditions for trapping and detachment of microscale air bubbles on the pure water freezing front. Langmuir *40*, 25334–25343. https://doi.org/10.1021/acs.langmuir.4c03815.
33. Carras, J.N., and Macklin, W.C. (1975). The opacity of accreted ice. Q. J. R. Meteorol. Soc. *101*, 203–206. https://doi.org/10.1023/B:HITE.0000020103.82678.13.
34. Shao, K., Song, M., Cai, B., Zhang, L., Pekař, L., and Zhang, X. (2024). Effects of environmental temperature and trapped air bubbles on the mechanical properties of ice cubes. ACS Appl. Mater. Interfaces *16*, 63482–63494. https://doi.org/10.1021/acsami.4c12227.
35. Shao, K., Zhen, Z., Gao, R., Song, M., Zhang, L., and Zhang, X. (2024). Comparative experimental study of the effect of loading rate on the typical mechanical properties of bubble and clear ice cubes. Exp. Therm. Fluid Sci. *159*, 111264. https://doi.org/10.1016/j.expthermflusci.2024.111264.
36. Wengrove, M.E., Pettit, E.C., Nash, J.D., Jackson, R.H., and Skyllingstad, E.D. (2023). Melting of glacier ice enhanced by bursting air bubbles. Nat. Geosci. *16*, 871–876. https://doi.org/10.1038/s41561-023-01262-8.
37. Barnola, J.M., Raynaud, D., Korotkevich, Y.S., and Lorius, C. (1987). Vostok ice core provides 160,000-year record of atmospheric CO2. Nature *329*, 408–414. https://doi.org/10.1038/329408a0.
38. Yamamoto, T. (2024). Bubble shape instability of acoustic cavitation in molten metal used in ultrasonic casting. Ultrason. Sonochem. *111*, 107064. https://doi.org/10.1016/j.ultsonch.2024.107064.
39. Li, Y. (2024). Are bubbles in ice the potential space for hydrogen storage? Int. J. Hydrogen Energ. *50*, 575–585. https://doi.org/10.1016/j.ijhydene.2023.07.273.
40. Deng, H., Guo, L., Wu, G., Chen, Z., Abbas, F., and Yin, Q. (2025). Preparation and evaluation of ozone micro-nano bubbles ice for Litchi precooling. Food Chem. *472*, 142945. https://doi.org/10.1016/j.foodchem.2025.142945.
41. Matsumoto, K., Zhang, S., Sekine, K., and Kubota, H. (2016). Investigation on influence of dimensions of ice containing ozone micro-bubbles on characteristics of ozone concentration. Int. J. Refrig. *66*, 41–49. https://doi.org/10.1016/j.ijrefrig.2016.02.017.